Thermionic Emission and Tunneling at Carbon Nanotube–Organic Semiconductor Interface

Biddut K. Sarker[†,‡] and Saiful I. Khondaker[†,‡,§,*]

[†]Nanoscience Technology Center, [‡]Department of Physics, and [§]School of Electrical Engineering and Computer Science, University of Central Florida, 12424 Research Parkway, Suite 400, Orlando, Florida 32826, United States

ABSTRACT

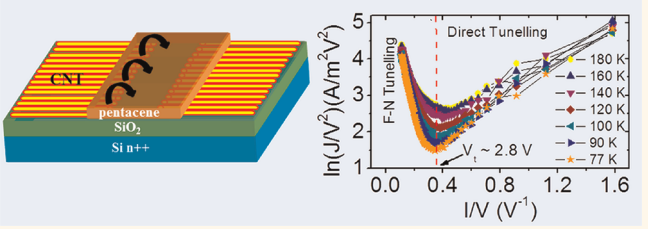

We study the charge carrier injection mechanism across the carbon nanotube (CNT)–organic semiconductor interface using a densely aligned carbon nanotube array as electrode and pentacene as organic semiconductor. The current density–voltage (J–V) characteristics measured at different temperatures show a transition from a thermal emission mechanism at high temperature (above 200 K) to a tunneling mechanism at low temperature (below 200 K). A barrier height of ~0.16 eV is calculated from the thermal emission regime, which is much lower compared to the metal/pentacene devices. At low temperatures, the J–V curves exhibit a direct tunneling mechanism at low bias, corresponding to a trapezoidal barrier, while at high bias the mechanism is well described by Fowler–Nordheim tunneling, which corresponds to a triangular barrier. A transition from direct tunneling to Fowler–Nordheim tunneling further signifies a small injection barrier at the CNT/pentacene interface. Our results presented here are the first direct experimental evidence of low charge carrier injection barrier between CNT electrodes and an organic semiconductor and are a significant step forward in realizing the overall goal of using CNT electrodes in organic electronics.

KEYWORDS: carbon nanotube electrodes · organic semiconductor · charge injection · barrier height · thermionic emission · Fowler–Nordheim tunneling · direct tunneling

Due to a large interfacial contact barrier, one of the major problems in the fabrication of high-performance organic electronic devices is inefficient charge injection from a metal electrode into organic semiconductors (OSC).[1–5] When the metal electrodes are contacted with the OSC, interfacial barriers such as a Schottky barrier and a dipole barrier are formed at the metal–OSC interface.[6–9] To be injected into the OSC, the charge carriers must overcome the large interface potential barrier by either thermal emission or tunneling.[10–14] A decrease in barrier height and width will improve the charge injection, which in turn will have significant impact in fabricating high-performance organic electronic devices. Due to their unique electronic properties, carbon nanotubes (CNTs) are considered to be a promising electrode material that can overcome the limitations of metal electrodes.[15–22] Recent room-temperature studies by our group and others have shown that, compared to organic field effect transistors (OFETs) using standard metal electrodes, OFETs using CNT electrodes have better mobility and higher on-current.[17–22] It is speculated that such improved device performance may be due to the improved injection of charge carriers from CNT to OSC owing to strong π–π bonding between the CNTs and OSC.[18,23] Although metal/OSC contact has been studied in great detail, very little information has been reported on the nature of CNT/OSC contact. In particular, there is no information about the barrier height or charge injection mechanism at the CNT/OSC interface. Such understanding can be obtained from a low-temperature transport study and is of great importance for achieving the overreaching goal of the CNT electrodes in organic electronics.

In this paper, we study the charge carrier injection mechanism at the CNT electrode–pentacene interface using temperature-dependent electronic transport measurements and provide direct evidence of low charge carrier injection barrier. We show that the current density–voltage (J–V) characteristics of the device above 200 K are well described by the Richardson–Schottky (RS) model, indicating that charge carrier injection is dominated by thermal emission in the high temperature regime.

* Address correspondence to saiful@ucf.edu.

Received for review February 6, 2012 and accepted May 4, 2012.

Published online May 04, 2012
10.1021/nn300544v

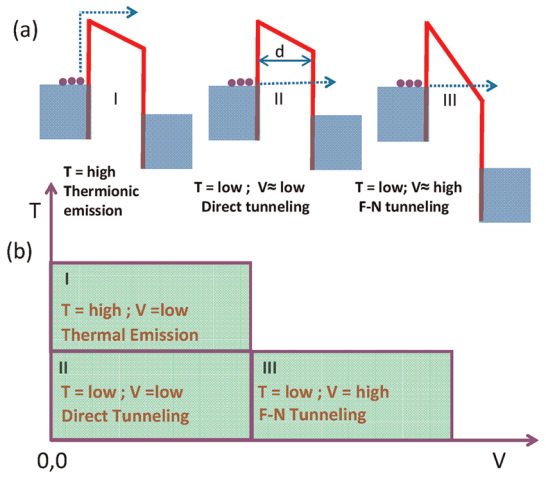

Figure 1. (a) Schematic diagram of a interfacial barrier at different temperatures and voltages. The circles represent the charge carriers, and the arrow indicates the charge carrier injection processes: (I) thermionic emission, (II) direct tunneling, and (III) Fowler–Nordheim (F–N) tunneling. (b) Typical phase diagram of transport regimes at various temperature and voltages.

We calculated a barrier height (φ_B) of 0.16 eV of the CNT/pentacene, which is much lower compared to the reported value of gold/pentacene as well as our control Pd/pentacene devices. We also show that the charge carrier injection mechanism crosses over from thermal emission to tunneling mechanism below 200 K, where charge injection is weakly temperature dependent. The *J*–*V* characteristics show a transition from direct tunneling at low bias to a Fowler–Nordheim (F–N) tunneling mechanism at high bias, further confirming a low charge injection barrier at the CNT/pentacene interface.

RESULTS AND DISCUSSION

A schematic diagram of a typical interface at different temperatures (*T*) and bias voltages (*V*) is shown in Figure 1a considering a simple rigid band model. Depending upon the temperature and bias voltage, different transport phenomena can occur as described by the phase diagram of Figure 1b. At low bias voltage and sufficiently high temperature, a large number of thermally activated charge carriers can overcome the barrier height (φ_B) in a classical way, resulting in thermionic emission (Figure 1a, I).[13,14] If the barrier height is large, this kind of emission will occur at temperatures higher than room temperature, whereas for a low barrier height thermionic emission can occur even at low temperatures. The *J*–*V* characteristics in this regime can be modeled using the RS equation for thermionic emission:[13]

$$J = A^*T^2 \exp\left[\frac{-(\Phi_B - \sqrt{q^3V/4\pi\varepsilon_0\varepsilon_r d})}{k_bT}\right] \quad (1)$$

where A^* is effective Richardson constant, ε_r is the permittivity of the OSC, ε_0 is the permittivity of the vacuum, q is the electron charge, and d is the width of the interface barrier. The barrier height (φ_B) can be directly calculated from the thermal emission regime by recognizing that at $V = 0$ V, $J = J_0 = A^*T^2 \exp(-\Phi_B/k_bT)]$. Therefore, a plot of $\ln(J_0/T^2)$ *versus* T^{-1} will show an activated behavior and the slope will give the value for φ_B.[24]

When the temperature decreases, there may not be enough thermal energy for the charge carriers to overcome the barrier height and the charge injection is dominated by tunneling through the interface barrier.[13,14,25] With increasing bias voltage, the shape of the tunnel barriers changes from trapezoidal (II in Figure 1a) to triangular (III in Figure 1a).[26] At low bias voltage, the tunnel barrier is trapezoidal (Figure 1a, II), and the *J*–*V* relation is described by teh direct tunneling mechanism:[13]

$$J \propto V\exp\left[-\frac{2d\sqrt{2m\Phi_B}}{\hbar}\right] \quad (2)$$

where $\hbar$ is Planck's constant divided by 2π and m is the effective mass of the charge carrier. When the bias voltages exceed the barrier height, the tunnel barrier becomes triangular (Figure 1a, III), and the *J*–*V* relation is described by Fowler–Nordheim (F–N) tunneling:[13]

$$J \propto V^2 \exp\left[-\frac{4d\sqrt{2m\Phi_B{}^3}}{3\hbar qV}\right] \quad (3)$$

The above *J*–*V* relations in eq 2 and eq 3 can be linearized in a logarithm scale to become eq 4 and eq 5, respectively:

$$\ln\left(\frac{J}{V^2}\right) \propto \ln\left(\frac{1}{V}\right) - \frac{2d\sqrt{2m\Phi_B}}{\hbar} \quad (4)$$

$$\ln\left(\frac{J}{V^2}\right) \propto -\left(\frac{1}{V}\right)\left(\frac{4d\sqrt{2m\Phi_B{}^3}}{3\hbar q}\right) \quad (5)$$

Therefore, a plot of $\ln(J/V^2)$ against $1/V$ will show logarithmic dependence in the direct tunneling (low bias) regime and linear dependence with a negative slope in the F–N tunneling (high bias) regime with an inflection point, describing the transition from direct to F–N tunneling regime. In cases of interfaces with large barrier height and width, only F–N tunneling can be observed and no measurable current can be detected before the onset of F–N tunneling, whereas for the interface with a small barrier height and width, both direct and F–N tunneling can be observed with a transition from one regime to another.[27] Therefore, a transition from direct tunneling to F–N tunneling is a hallmark of low interfacial barrier[27] and has not been observed in the metal/OSC interface, where the interface barrier is large.

To examine the charge injection mechanism at the CNT/OSC interface, we fabricated single-walled carbon

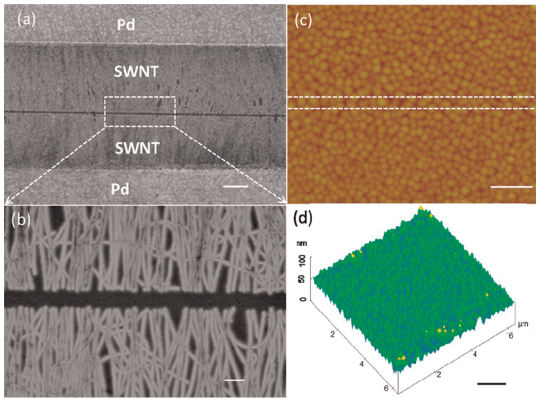

Figure 2. (a) SEM image of part of the densely aligned SWNT source and drain electrodes. The SWNTs were assembled *via* dielectrophoresis. The SWNTs source and drain electrodes were fabricated through oxidative cutting of a densely aligned SWNT array by EBL and precise oxygen plasma etching. (b) High-magnification image of (a). Tapping mode AFM (c) height and (d) surface image of the deposited pentacene thin film. The white region marks the channel area defined by the SWNT electrodes where pentacene is deposited onto the SiO_2 substrate. The scale bars in parts (a), (c), and (d) are 1 μm, and that in (b) is 200 nm.

nanotube (SWNT) source and drain electrodes through dielectrophoretic (DEP) assembly of SWNTs in a dense array and oxidative cutting of the SWNT array by electron beam lithography (EBL) followed by precise oxygen plasma etching. The details of the SWNT assembly and electrode fabrication can be found in our recent publications.[17−19,28] In brief, we used heavily doped Si substrates with a thermally grown 250 nm thick SiO_2 layer as a substrate. Palladium (Pd) patterns of 5 μm × 25 μm, fabricated by optical lithography, were used to align the nanotubes *via* ac DEP from a high-quality, stable, and surfactant-free SWNT aqueous solution. For this study, we fabricated five samples with 24−30 SWNT/μm in the array. (See Figure 1a, b and Supporting Information Figures S1 and S2.) The resistances of the assembled SWNT arrays were in the range 400−800 Ω with corresponding sheet resistances of 1.5−3 KΩ/□, making them suitable as an electrode material. After the assembly, SWNT source and drain electrodes of channel length L = 200 nm and width W = 25 μm were fabricated by defining a window using the standard EBL process and oxygen plasma etching of the exposed nanotubes inside the window.

Figure 2a shows a scanning electron microscopy (SEM) image of a part of the SWNT source and drain electrodes. Figure 2b shows a high-magnification image of the electrode. From this image, we calculate 68 SWNTs in a 2.8 μm long image, giving a linear density of 24 SWNTs/μm. The nanotubes are swollen due to the low kV imaging. Figure 1b also shows that most of the nanotubes in the electrodes are well aligned with open-ended tips (see also AFM image in Supporting Information Figure S2). Finally, we deposited a pentacene thin film of 30 nm by thermal evaporation.

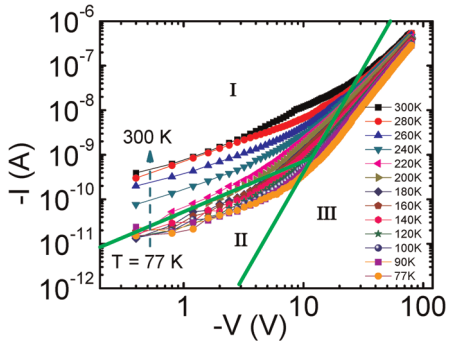

Figure 3. Log−log plot of the current−voltage (I−V) characteristics of the SWNT/pentacene device in the temperature range 300−77 K at zero gate voltage. I, II, and III indicate the three different charge transport regimes depending on T and V (marked by solid green lines). I, II, and III correspond to the regimes described in Figure 1.

Figure 2c and d show a part of the height and surface view of the AFM image of the deposited pentacene film morphology. The morphology of the pentacene film within the channel on a SiO_2 substrate slightly differs from the morphology of pentacene on the nanotube electrodes. The pentacene grain size on the nanotube electrodes is ∼140−160 nm with a surface roughness of ∼3 nm, whereas the pentacene grain size within the channel on the SiO_2 substrate is ∼170−190 nm with a surface roughness of ∼4.2 nm (see Supporting Information Figure S3). For this study, we chose L = 200 nm because at this channel length the contact resistance is much more dominating over the channel resistance (see Supporting Information Figure S4), so that the charge transport characteristics will be dominated by contact. Another reason for choosing as small a channel length as possible is to reduce the number of grain boundaries in the active material. It is well known that the conductivity of the OSC is limited by the grain boundaries, and the strong temperature dependence of the resistance and mobility of the OSC arises from the grain boundaries.[29,30] In larger channel length devices, there are many grain boundaries and the conductivity of the OSC is dominated by them. On the other hand, for a very short channel length device, there are only a few grain boundaries and the conductivity is dominated by contact. Since the average grain size of the pentacene in our devices is about 180 nm, there will be only one grain boundary on average along the channel of our device (see Figure 2c), making these devices appropriate for studying interface effects. The devices were then bonded and loaded into a cryostat for low-temperature transport measurements. A total of five devices were measured.

Figure 3 shows current−voltage (I−V) characteristics of a representative device at zero gate voltage plotted in a log−log scale measured at different temperatures from 300 to 77 K (see Supporting Information Figure S5 for room-temperature OFET characteristics). It can be

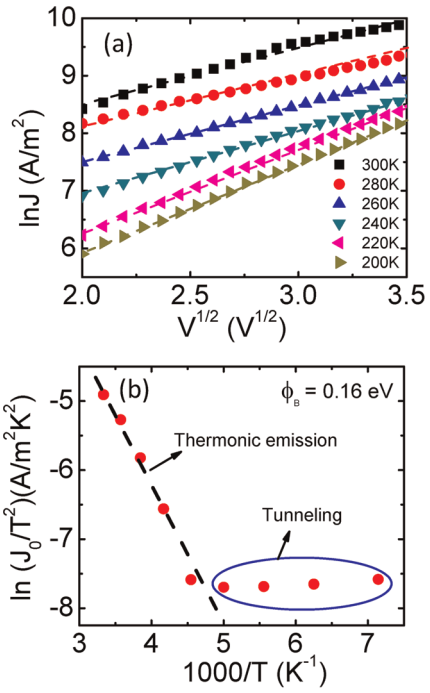

Figure 4. (a) ln(*J*) *versus* $V^{1/2}$ plot of the *I*−*V* data at 300 to 200 K (regime I in Figure 3). The current densities at zero bias voltage (J_0) were obtained by extrapolating of the ln(*J*) curve at *V* = 0 V. (b) Relation between ln(J_0/T^2) and 1/*T*. From the slope of the dotted line the interfacial energy barrier height at the SWNT/pentacene interface is determined to be 0.16 eV.

seen from this figure that the current strongly depends on both the temperature and voltage. Three interesting features can be seen in this figure. At high temperature (above 200 K) and low bias voltage (regime I), the *I*−*V* curves strongly depend on the temperature, indicating thermally activated charge injection mechanism.[13,14] At low temperature (<200 K), the *I*−*V* curves show a weakly temperature-dependent phenomenon with current either weakly voltage dependent (regime II) or strongly voltage dependent (regime III), which can be well described by the tunneling mechanism.[14,25]

The strongly temperature-dependent *I*−*V* curves in regime I can be well described by the RS model for thermionic emission, eq 1. This is shown in Figure 4a, where we plot ln *J* against $V^{1/2}$ for temperatures above 200 K. As expected from the RS model (ln $J \propto V^{1/2}$), all the curves show a straight line with positive slope. These data also allow for the calculation of barrier height (Φ_B) at the SWNT/pentacene interface. In order to calculate the Φ_B, we first determined J_0 as a function of the temperature by extrapolating the straight lines of Figure 4a to *V* = 0 V and plotted ln(J_0/T^2) as a function of 1/*T* in Figure 4b. This figure clearly shows that the ln(J_0/T^2) *versus* 1/*T* plot follows a linear relation with negative slope at higher temperature range (above 200 K), denoted by the dotted line. However, this plot deviates from the linear relation and becomes weakly temperature-dependent at lower temperature (below 200 K). This is consistent with Figure 3, regions II and III, where we saw weakly temperature-dependent *I*−*V* curves, and signifies a transition from thermionic emission to tunneling mechanism. This transition phenomenon of our devices can be easily understood. At high temperature, a large number of charge carriers have energies large enough to cross the barrier height in a classical way.[14] However, when the temperature decreases, the energies of the charge carriers become low, which may not be sufficient enough to overcome the barrier height and hence the thermionic emission stops. The charge injection only then occurs quantum mechanically by tunneling.[14,25]

We calculated a barrier height of 0.16 eV at the SWNT/pentacene interface from the slope of ln(J_0/T^2) *versus* 1/*T* plot in Figure 4b. We have measured and analyzed five SWNT/pentacene devices in this study, and all the devices have shown similar transport characteristics (see Supporting Information Figure S6). The calculated barrier height of the SWNT/pentacene interface is significantly lower than that of the reported barrier height of 0.5−0.85 eV at the gold/pentacene interface measured by different groups[6,31,32] as well as our control Pd/pentacene device, where we obtained a barrier height of 0.35 eV (see Supporting Information Figure S7). Interestingly, our measured barrier height at SWNT/pentacene is also similar to the barrier height reported for the graphene/pentacene interface.[33] We note that we did not apply any V_g in the temperature-dependent *I*−*V* characteristics of our devices to extract the true barrier height at the SWNT/OSC interface.[12,14] It has been reported that the Schottky barrier can be significantly reduced by applying V_g, and a barrier height measured at V_g other than 0 V is not a true barrier height.[12,14] In addition, a finite V_g also reduces the tunnel barrier width in the tunneling regime, enhancing the tunnel current.[14]

In previous room-temperature transport studies of the SWNT-contacted OFET devices, better charge mobility and higher on-current were reported compared to the metal-contacted devices.[17−22] It was speculated that the better performance was due to improved charge injection at the SWNT/OSC. However, no direct evidence of the barrier height at the SWNT/OSC was reported. Our study shows for the first time that a low charge injection barrier indeed exists at the SWNT/OSC interface. The work functions for Pd and Au are 5.1 eV, and it is 5.0 eV for SWNT,[19,34] while the highest occupied molecular orbital (HOMO) level of the pentacene is 5.1 eV.[32] Although the work function of the metal (Pd, Au) and SWNT matches with the HOMO level of the pentacene, a significant barrier exists between the metal and pentacene interface. It has been reported that when pentacene is contacted with a gold electrode, pentacene is physisorped onto the gold surface, leading to the formation of dipole barriers at Au/pentacene interfaces.[6−9] This gives rise to

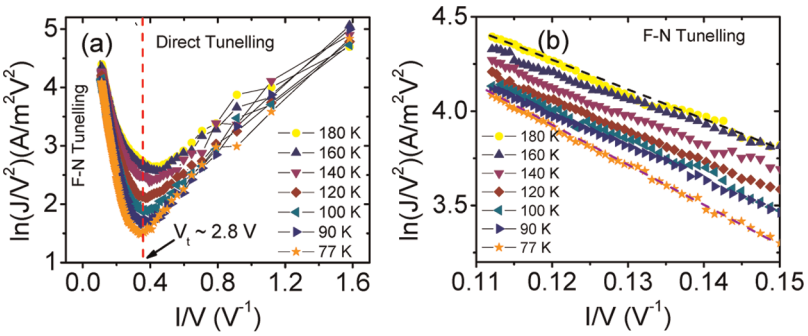

Figure 5. ln(J/V^2) *versus* 1/V plot of the data for weakly temperature-dependent $I-V$ data at 180−77 K (regimes II and III in Figure 3). The curves show a transition from direct tunneling to F−N tunneling with a voltage inflection point. (b) Magnified view of the ln(J/V^2) *versus* 1/V plot, showing the linear behavior between them, in agreement with F−N tunneling.

a "push back" effect, a decrease of surface dipole potential energy of the gold surface in contact with the OSC.[8,9,35] As a result, the effective work function of gold electrodes reduces to 4.5 eV, giving rise to a large Schottky barrier for hole injection. Similar work function lowering may also occur for Pd/pentacene devices. In contrast, a strong $\pi-\pi$ interaction exists between the SWNT and pentacene.[23] Therefore, significant dipole formation may not occur and the work function of the SWNT may not be modified in contact with OSC, causing the barrier to remain low.

In Figure 4b, we observed a deviation from the RS model at temperatures below 200 K, possibly due to a transition from thermionic emission to tunneling. In order to confirm that tunneling is indeed the injection mechanism, we analyzed our low-temperature data using both the direct tunneling and F−N tunneling models. We mentioned earlier that a plot of ln(J/V^2) *versus* 1/V will show logarithmic dependence in the direct tunneling (low bias) regime and linear dependence with a negative slope in the F−N tunneling (high bias) regime with an inflection point describing the transition from the direct to F−N tunneling regime. Such a transition from direct to F−N tunneling is a hallmark of low interfacial barrier.[27] Figure 5a shows a plot of the ln(J/V^2) versus 1/V in the temperatures range 180−77 K. The most important feature of this figure is that all the curves show two distinct transport regimes with voltage inflection points (V_t). The V_t of this devices is 2.8 V (1/$V \approx 0.35$ V^{-1}). When $V > 2.8$ V, we observed a linear relationship of the ln(J/V^2) *versus* 1/V curves with negative slope for all temperatures. This is more clearly shown in Figure 5b and is consistent with the F−N tunneling model, eq 5. From the slope of the ln(J/V^2) *versus* 1/V curves and using a barrier height of 0.16 eV, we have calculated a barrier width $d \approx 20$ nm of the SWNT/pentacene interface. However when $V < 2.8$ V, the transport characteristics change and the curves cross over to a logarithmic dependence in 1/V, in agreement with direct tunneling, eq 4. This is more clearly shown in supplementary Figure S8. Therefore, from these results we confirm that the charge carrier injection of our device is dominated by direct tunneling at voltages less than the transition voltage and by F−N tunneling at voltages higher than the transition voltage. In addition, the exhibition of the inflection point in the ln(J/V^2) *versus* (1/V) plots in Figure 5a provides a signature of a transition from direct tunneling to F−N tunneling in our devices. This confirms a change of the barrier shape at the SWNT/pentacene interface from trapezoidal to triangular with increasing bias voltage, as illustrated by the band energy diagram in Figure 1.

The transition from the direct tunneling to F−N tunneling was not observed in the devices that have sustainable interfacial barrier height and width.[27] Although F−N tunneling has been reported in organic devices fabricated with metal electrodes,[29,36−38] the direct tunneling as well as the transition from direct to F−N tunneling has not been observed in these devices. This is due to the existence of a high barrier width at the metal/OSC interfaces. In contrast, we observed a transition from direct tunneling to F−N tunneling of our devices fabricated with a SWNT electrode along with a low barrier height, which confirms that interfacial barrier height and width of the SWNT/pentacene interface are very small.

CONCLUSIONS

In conclusion, we studied the charge injection mechanism at the SWNT/pentacene interface by using temperature-dependent electronic transport measurement of pentacene devices fabricated using SWNT electrodes. In the temperature range 300−200 K, the charge injection mechanism is dominated by thermal emission, which is well explained by the RS model. The calculated barrier height at SWNT/pentacene interfaces is smaller than the barrier height at metal/pentacene interfaces. We observed a transition from thermal emission to the tunneling mechanism at temperatures below 200 K. In addition, at low temperature

the current–voltage characteristics show a transition from direct tunneling to Fowler–Nordheim tunneling, which suggests that the barrier width at the SWNT/pentacene interface is very small.

MATERIALS AND METHODS

Fabrication of the SWNT Electrodes. SWNTs of high density were aligned between palladium patterns of 5 μm separation *via* ac dielectrophoresis in a probe station. The Pd patterns were fabricated by photolithography followed by thermal evaporation of Pd with a thinness of 30 nm and standard lift-off. We obtained a highly purified, stable, and surfactant-free SWNT solution suspended in water from Brewer Science Inc. The details of the assembly of the SWNT and SWNT electrode fabrication can be found in refs 17–19 and 28. In brief, the concentration of the original solution was 50 μg/mL, and it was diluted by six times in deionized (DI) water. A 3 μL drop of the solution was placed on the chip, and an ac voltage of 5 $V_{p\text{-}p}$ at 300 kHz was applied between the Pd patterns for 30 s. The ac voltage creates a time DEP force between Pd patterns and aligns the SWNTs. After alignment, PMMA was spin coated on the samples at 4000 rpm for 60 s followed by baking at 180 °C for 15 min on a hot plate. A precise window of electrode patterns was opened by EBL writing and developing in a mixture of MIBK and IPA. The EBL was done by a Zeiss Ultra-55 SEM combined with a Nabity pattern generator. After that, the samples were put in the oxygen plasma cleaner to etch the exposed SWNT array through the open window. Finally, samples were kept in the chloroform for 12 h and rinsed with acetone, IPA, ethanol, and DI water to remove the remaining PMMA. For the low-temperature study, we fabricated SWNT electrodes of L = 200 nm and W = 25 μm. In addition, to determine the room-temperature contact resistance of the SWNT/pentacene devices, we fabricated SWNT electrodes of L = 200, 700 nm, 2, 3, 4 μm with W = 25 μm. We also fabricated Pd electrodes of L = 200 nm and W = 25 μm for a control experiment.

Deposition of Pentacene Film. Pentacene was deposited by thermal evaporation at a pressure 2×10^{-5} Pa onto both aligned array electrodes and Pd electrodes. The pentacene film deposition rate was 0.2 Å/s, and the thickness of the film was 30 nm, measured by AFM. We note that in this experiment we did not perform any surface treatment of our devices.

Characterization of the Devices. The SEM images of the SWNT electrodes were taken on a Zeiss Ultra-55 SEM, and trapping mode AFM images of the SWNT electrode and pentacene thin film were acquired by using a Dimension 3100 AFM (Veeco). The electrical transport measurements of the SWNT array and SWNT electrodes were carried out by a DL Instruments 1211 current preamplifier and a Keithley 2400 source meter interfaced with the LabView program. The OFET characteristics were measured using a Hewlett-Packed 4145B semiconductor parametric analyzer. We measured I–V characteristics of our devices at different temperatures in the range 300 to 77 K. In order to take reproducible measurements at each temperature, we measured each I–V curve at least two times and waited 15 min between successive measurements. The temperature was controlled with a Lakeshore temperature controller, and we waited at least 10 min to stabilize the temperature before taking data.

Conflict of Interest: The authors declare no competing financial interest.

Acknowledgment. This work is supported by the U.S. National Science Foundation under Grant ECCS 1102228.

Supporting Information Available: (1) SWNT assembly and characterization. (2) Characterization of SWNT electrodes. (3) Morphology of pentacene film. (4) Contact resistance at SWNT/pentacene interface. (5) Room-temperature FET characteristics of the SWNT/pentacene and Pd/pentacene devices. (6) Temperature-dependent transport properties of another SWNT/pentacene device. (7) Barrier height of Pd/pentacene device. (8) Direct tunneling. This material is available free of charge *via* the Internet at http://pubs.acs.org.

REFERENCES AND NOTES

1. Liu, Z.; Kobayashi, M.; Paul, B. C.; Bao, Z.; Nishi, Y. Contact Engineering for Organic Semiconductor Devices *via* Fermi Level Depinning at the Metal-Organic Interface. *Phys. Rev. B* **2010**, *82*, 035311.
2. Burgi, L.; Richards, T. J.; Friend, R. H.; Sirringhaus, H. Close Look at Charge Carrier Injection in Polymer Field-Effect Transistors. *J. Appl. Phys.* **2003**, *94*, 6129–6137.
3. Thakur, A. K.; Mukherjee, A. K.; Preethichandra, D. M. G.; Takashima, W.; Kaneto, K. Charge Injection Mechanism across the Au-Poly(3-hexylthiophene-2,5-diyl) Interface. *J. Appl. Phys.* **2007**, *101*, 104508.
4. Gundlach, D. J.; Zhou, L.; Nichols, J. A.; Jackson, T. N.; Necliudov, P. V.; Shur, M. S. An Experimental Study of Contact Effects in Organic Thin Film Transistors. *J. Appl. Phys.* **2006**, *100*, 024509.
5. Scott, J. C. Metal-Organic Interface and Charge Injection in Organic Electronic Devices. *J. Vac. Sci. Technol. A* **2003**, *21*, 521–531.
6. Koch, N.; Kahn, A.; Ghijsen, J.; Pireaux, J. J.; Schwartz, J.; Johnson, R. L.; Elschner, A. Conjugated Organic Molecules on Metal *versus* Polymer Electrodes: Demonstration of a Key Energy Level Alignment Mechanism. *Appl. Phys. Lett.* **2003**, *82*, 70–72.
7. Hill, I. G.; Rajagopal, A.; Kahn, A.; Hu, Y. Molecular Level Alignment at Organic Semiconductor-Metal Interfaces. *Appl. Phys. Lett.* **1998**, *73*, 662–664.
8. Braun, S.; Salaneck, W. R.; Fahlman, M. Energy-Level Alignment at Organic/Metal and Organic/Organic Interfaces. *Adv. Mater.* **2009**, *21*, 1450–1472.
9. Ishii, H.; Sugiyama, K.; Ito, E.; Seki, K. Energy Level Alignment and Interfacial Electronic Structures at Organic/Metal and Organic/Organic Interfaces. *Adv. Mater.* **1999**, *11*, 605–625.
10. Chiguvare, Z.; Parisi, J.; Dyakonov, V. Current Limiting Mechanisms in Indium-Tin-Oxide/Poly3-Hexylthiophene/Aluminum Thin Film Devices. *J. Appl. Phys.* **2003**, *94*, 2440–2448.
11. Barth, S.; Wolf, U.; Bässler, H.; Müller, P.; Riel, H.; Vestweber, H.; Seidler, P. F.; Rieß, W. Current Injection from a Metal to a Disordered Hopping System. iii. Comparison Between Experiment and Monte Carlo Simulation. *Phys. Rev. B* **1999**, *60*, 8791–8797.
12. Appenzeller, J.; Radosavljević, M.; Knoch, J.; Avouris, P. Tunneling *versus* Thermionic Emission in One-Dimensional Semiconductors. *Phys. Rev. Lett.* **2004**, *92*, 048301.
13. Wang, W.; Lee, T.; Reed, M. A. Mechanism of Electron Conduction in Self-Assembled Alkanethiol Monolayer Devices. *Phys. Rev. B* **2003**, *68*, 035416.
14. Svensson, J.; Campbell, E. E. B. Schottky Barriers in Carbon Nanotube-Metal Contacts. *J. Appl. Phys.* **2011**, *110*, 111101.
15. Guo, X.; Small, J. P.; Klare, J. E.; Wang, Y.; Purewal, M. S.; Tam, I. W.; Hong, B. H.; Caldwell, R.; Huang, L.; O'Brien, S.; *et al.* Covalently Bridging Gaps in Single-Walled Carbon Nanotubes with Conducting Molecules. *Science* **2006**, *311*, 356–359.
16. Qi, P. F.; Javey, A.; Rolandi, M.; Wang, Q.; Yenilmez, E.; Dai, H. J. Miniature Organic Transistors with Carbon Nanotubes as Quasi-One-Dimensional Electrodes. *J. Am. Chem. Soc.* **2004**, *126*, 11774–11775.
17. Sarker, B. K.; Khondaker, S. I. High-Performance Short Channel Organic Transistors Using Densely Aligned Carbon Nanotube Array Electrodes. *Appl. Phys. Lett.* **2012**, *100*, 023301.
18. Sarker, B. K.; Liu, J.; Zhai, L.; Khondaker, S. I. Fabrication of Organic Field Effect Transistor by Directly Grown Poly(3 hexylthiophene) Crystalline Nanowires on Carbon Nanotube Aligned Array Electrode. *ACS Appl. Mater. Interfaces* **2011**, *3*, 1180–1185.

19. Sarker, B. K.; Islam, M. R.; Alzubi, F.; Khondaker, S. I. Fabrication of Carbon Nanotube Electrode for Organic Electronics Devices. *Mater. Express* **2011**, *1*, 80–85.
20. Hellstrom, S. L.; Jin, R. Z.; Stoltenberg, R. M.; Bao, Z. Driving High-Performance n- and p-Type Organic Transistors with Carbon Nanotube/Conjugated Polymer Composite Electrodes Patterned Directly from Solution. *Adv. Mater.* **2010**, *22*, 4204–4208.
21. Aguirre, C. M.; Ternon, C.; Paillet, M.; Desjardins, P.; Martel, R. Carbon Nanotubes as Injection Electrodes for Organic Thin Film Transistors. *Nano Lett.* **2009**, *9*, 1457–1461.
22. Cicoira, F.; Aguirre, C. M.; Martel, R. Making Contacts to n-Type Organic Transistors Using Carbon Nanotube Arrays. *ACS Nano* **2010**, *5*, 283–290.
23. Chia-Hao, C.; Chao-Hsin, C.; Jung-Yen, Y. Pentacene-Based Thin-Film Transistors With Multiwalled Carbon Nanotube Source And Drain Electrodes. *Appl. Phys. Lett.* **2007**, *91*, 083502.
24. Aboelfotoh, M. O.; Fröjdh, C.; Petersson, C. S. Schottky-Barrier Behavior of Metals on N- and P-type 6h-Sic. *Phy. Rev. B* **2003**, *67*, 075312.
25. Worne, J. H.; Anthony, J. E.; Natelson, D. Transport in Organic Semiconductors in Large Electric Fields: from Thermal Activation to Field Emission. *Appl. Phys. Lett.* **2010**, *96*, 053308.
26. Araidai, M.; Tsukada, M. Theoretical Calculations of Electron Transport in Molecular Junctions: Inflection Behavior in Fowler-Nordheim Plot and Its Origin. *Phys. Rev. B* **2010**, *81*, 235114.
27. Beebe, J. M.; Kim, B.; Gadzuk, J. W.; Daniel Frisbie, C.; Kushmerick, J. G. Transition from Direct Tunneling to Field Emission in Metal-Molecule-Metal Junctions. *Phys. Rev. Lett.* **2006**, *97*, 026801.
28. Shekhar, S.; Stokes, P.; Khondaker, S. I. Ultrahigh Density Alignment of Carbon Nanotube Arrays by Dielectrophoresis. *ACS Nano* **2011**, *5*, 1739–1746.
29. Horowitz, G. Tunneling Current in Polycrystalline Organic Thin-Film Transistors. *Adv. Funct. Mater.* **2003**, *13*, 53–60.
30. Horowitz, G.; Hajlaoui, M. E. Mobility in Polycrystalline Oligothiophene Field-Effect Transistors Dependent on Grain Size. *Adv. Mater.* **2000**, *12*, 1046–1050.
31. Schroeder, P. G.; France, C. B.; Park, J. B.; Parkinson, B. A. Orbital Alignment and Morphology of Pentacene Deposited on Au(111) and SnS_2 Studied Using Photoemission Spectroscopy. *J. Phys. Chem. B* **2003**, *107*, 2253–2261.
32. Diao, L.; Frisbie, C. D.; Schroepfer, D. D.; Ruden, P. P. Electrical Characterization of Metal/Pentacene Contacts. *J. Appl. Phys.* **2007**, *101*, 014510.
33. Lee, S.; Jo, G.; Kang, S.-J.; Wang, G.; Choe, M.; Park, W.; Kim, D.-Y.; Kahng, Y. H.; Lee, T. Enhanced Charge Injection in Pentacene Field-Effect Transistors with Graphene Electrodes. *Adv. Mater.* **2011**, *23*, 100–105.
34. Javey, A.; Guo, J.; Wang, Q.; Lundstrom, M.; Dai, H. Ballastic Carbon Nanotube Field-Effect Transistors. *Nature* **2003**, *424*, 654–657.
35. Osikowicz, W.; Jong, M. P. d.; Braun, S.; Tengstedt, C.; Fahlman, M.; Salaneck, W. R. Energetics at Au Top and Bottom Contacts on Conjugated Polymers. *Appl. Phys. Lett.* **2006**, *88*, 193504.
36. Hummelgen, I. A.; Roman, L. S.; Nart, F. C.; Peres, L. O.; Sa, E. L. d. Polymer and Polymer/Metal Interface Characterization *via* Fowler-Nordheim Tunneling Measurements. *Appl. Phys. Lett.* **1996**, *68*, 3194–3196.
37. Chiu, J. J.; Kei, C. C.; Perng, T. P.; Wang, W. S. Organic Semiconductor Nanowires for Field Emission. *Adv. Mater.* **2003**, *15*, 1361–1364.
38. Koehler, M.; Hummelgen, I. A. Temperature Dependent Tunnelling Current at Metal/Polymer Interfaces-Potential Barrier Height Determination. *Appl. Phys. Lett.* **1997**, *70*, 3254–3256.